CHEMISTRY OF MATERIALS

Article

In Situ Activation of an Indium(III) Triazenide Precursor for Epitaxial Growth of Indium Nitride by Atomic Layer Deposition

Nathan J. O'Brien,* Polla Rouf, Rouzbeh Samii, Karl Rönnby, Sydney C. Buttera, Chih-Wei Hsu, Ivan G. Ivanov, Vadim Kessler, Lars Ojamäe, and Henrik Pedersen

Cite This: *Chem. Mater.* 2020, 32, 4481–4489
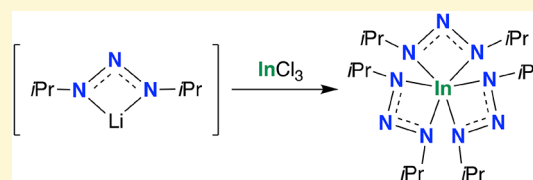
Read Online

ACCESS | Metrics & More | Article Recommendations | Supporting Information

ABSTRACT: Indium nitride (InN) is characterized by its high electron mobility, making it a ground-breaking material for high frequency electronics. The difficulty of depositing high-quality crystalline InN currently impedes its broad implementation in electronic devices. Herein, we report a new highly volatile In(III) triazenide precursor and demonstrate its ability to deposit high-quality epitaxial hexagonal InN by atomic layer deposition (ALD). The new In(III) precursor, the first example of a homoleptic triazenide used in a vapor deposition process, was easily synthesized and purified by sublimation. Thermogravimetric analysis showed single step volatilization with an onset temperature of 145 °C and negligible residual mass. Strikingly, two temperature intervals with self-limiting growth were observed when depositing InN films. In the high-temperature interval, the precursor underwent a gas-phase thermal decomposition inside the ALD reaction chamber to produce a more reactive In(III) compound while retaining self-limiting growth behavior. Density functional theory calculations revealed a unique two-step decomposition process, which liberates three molecules of each propene and N_2 to give a smaller tricoordinated In(III) species. Stoichiometric InN films with very low levels of impurities were grown epitaxially on 4H-SiC. The InN films deposited at 325 °C had a sheet resistivity of 920 Ω/sq. This new triazenide precursor enables ALD of InN for semiconductor applications and provides a new family of M−N bonded precursors for future deposition processes.

1. INTRODUCTION

The high electron mobility of indium nitride (InN)[1,2] makes it a very interesting material for the conduction channel in high electron mobility transistors (HEMTs) and high frequency electronics. InN can be integrated in state-of-the-art electronic devices that are based on aluminum- and gallium nitride (AlN and GaN) and their alloys, given the close similarities in their crystal lattices. The implementation of InN into device structures requires deposition of epitaxially orientated and stoichiometric InN thin films with negligible impurities on substrates with high thermal conductivity such as SiC.[3] The current chemical vapor deposition (CVD) processes used for depositing thin films of AlN and GaN, at high temperatures of 800−1000 °C, are not suitable for depositing InN as it decomposes to In metal and N_2 gas at approximately 500 °C.[4] This sets a strict upper temperature limit for CVD of InN where the reactivity of the nitrogen precursor, ammonia (NH_3), is very low, forcing N/In ratios in the order of 10^5 and thus poorly functioning CVD chemistry.[5,6] Atomic layer deposition (ALD) is a low temperature time-resolved form of CVD, in which the metal and nonmetal precursors are pulsed into the reaction chamber sequentially. This process allows for the deposition of the resulting film to be governed solely by surface chemical reactions.[7] The ALD cycle is repeated hundreds of times to deposit films with controlled thickness, excellent large-area uniformity, and conformity. We

envision that ALD is the way forward to realize electronics based on InN. Although ALD is routinely used in the production of modern electronic devices, its potential for InN is yet to be unlocked. This is mostly due to the poor deposition chemistry afforded at low temperatures by the commonly used trimethylindium ($InMe_3$) precursor. ALD of InN with $InMe_3$ and either N_2[8,9] or NH_3[10] plasma has produced epitaxial InN on GaN(0001), Si(111), and sapphire substrates[8,11,12] but renders films with high carbon and oxygen impurity levels and nonstoichiometric In/N ratios.

For successful ALD, it is important to have a metal precursor with high volatility and thermal stability that cleanly reacts with the surface to avoid unwanted byproducts.[7] Efforts have been made to develop In(III) precursors with favorable surface chemistry for ALD of InN by replacing the M−C bonds of $InMe_3$ with M−N bonds. Homoleptic tricoordinated M−N bonded compounds have been reported,[13−17] but these often require bulky ligands to stabilize the In center, which reduces their volatility. Instead, homoleptic hexacoordinated M−N
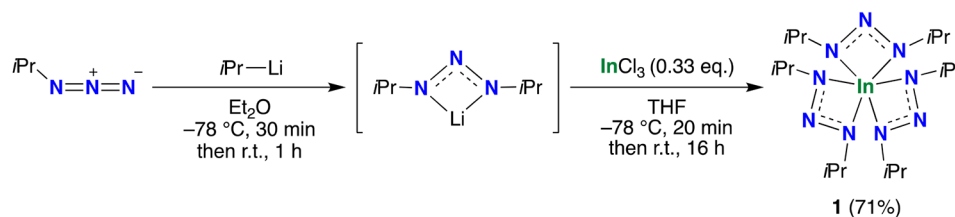
Scheme 1. Synthesis of Tris(1,3-diisopropyltriazenide)indium(III) 1.

1 (71%)

bonded precursors, In(III) tris-amidinate (In(amd)$_3$),[18] formamidinate (In(famd)$_3$),[19] and guanidinate (In-(guan)$_3$),[20,21] have shown increased thermal stability in comparison to tricoordinated In(III) precursors and were first used for ALD of In$_2$O$_3$[19,21] and In$_2$S$_3$.[22] Recently, we investigated these precursors with NH$_3$ plasma for ALD of crystalline InN.[23] The best results were achieved with In(famd)$_3$, giving the highest degree of crystallinity, lowest impurity levels, and an In/N ratio of 1.01. It was further revealed that smaller and less electron donating substituents on the endocyclic carbon of the amidinate ligand backbone led to an improved surface chemistry in ALD of InN films. To further explore this trend, we envisaged changing the endocyclic position to an even smaller and more electron-withdrawing moiety. A ligand that is closely related to the amidinates is the triazenide, which differs only by the electronegative nitrogen atom in the endocyclic position of the ligand backbone. Although the binding modes of amidinates are similar to those of triazenides, the extra nitrogen atom is thought to make the chelating nitrogens weaker binders.[24,25] This would benefit the surface reactions of the precursor during deposition by making the In−N bonds weaker and the In metal center more electrophilic. There are many examples of homoleptic triazenide complexes in the literature,[25−34] including an In(III) complex (In(dptriaz)$_3$);[35,36] however, these are undesirable for vapor deposition due to the 1,3-diphenyltriazenide ligand. Homoleptic 1,3-dimethyltriazenide[37] and heteroleptic 1-*tert*-butyl-3-alkyltriazenide[38,39] complexes have also been reported for various metals, but these suffer from low volatility and thermal stability. To the best of our knowledge, there are no examples of a homoleptic 1,3-dialkyltriazenide complex used for vapor deposition. Herein, we report the synthesis, structure, and physical properties of a new In(III) precursor, tris(1,3-diisopropyltriazenide)indium(III) **1**, and demonstrate it as an excellent ALD precursor for epitaxial InN thin films on 4H-SiC.

2. RESULTS AND DISCUSSION

2.1. Synthesis and Characterization of In(III) Triazenide Precursor. Reaction of isopropylazide[40] with isopropyllithium generated the lithium 1,3-diisopropyltriazenide intermediate, which was reacted directly with indium trichloride (InCl$_3$) at −78 °C to give tris(1,3-diisopropyltriazenide)indium(III) **1** in a 71% yield (Scheme 1). Compound **1** was isolated as a colorless solid after purification by sublimation. It was found to be highly stable at room temperature in both solid and solution states under an inert atmosphere; however, exposure to air led to decomposition to a white insoluble powder thought to be of In$_2$O$_3$. The compound was characterized by nuclear magnetic resonance (NMR) spectroscopy, mass spectrometry (MS), elemental analysis, and X-ray crystallography.

The crystal structure of **1** (Figure 1, Tables S1−S5) showed the In atom in a distorted-octahedral coordination geometry
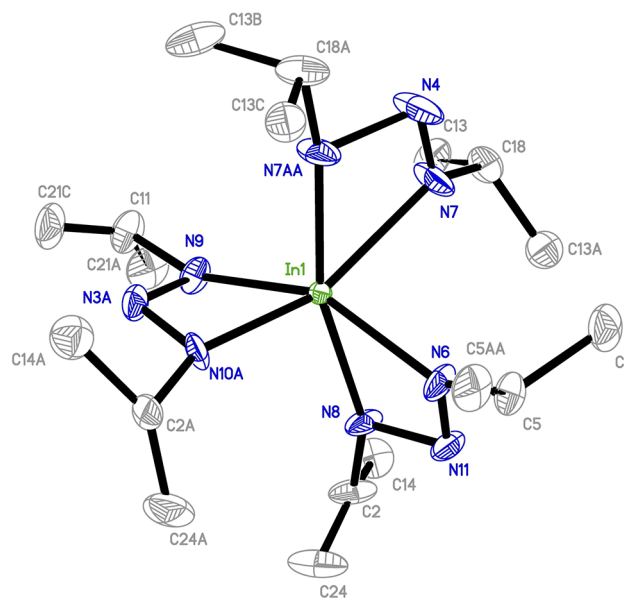

Figure 1. ORTEP drawing of **1** with thermal ellipsoids at the 50% probability level. All hydrogen atoms were removed for clarity.

with the triazenide ligands in a pseudo-C_3 propeller arrangement similarly to the previously reported In(dptriaz)$_3$.[36] Two of the ligands were found to be distorted over four positions and the third over two positions. The In−N bond lengths (av. 2.21(5) Å) were similar to that of In(dptriaz)$_3$ (av. 2.237(6) Å),[36] In(famd)$_3$ (av. 2.252(13) Å),[19] In(amd)$_3$ (av. 2.236(1) Å),[18] and In(guan)$_3$ (av. 2.260(4) Å),[20,21] showing that the alkyl-triazenide ligand has little effect on the In−N bond distances.

The ^{1}H NMR spectrum of **1** in C$_6$D$_6$ showed one septet at 4.06 ppm and one doublet at 1.23 ppm for the methine proton and methyl groups of the isopropyl moiety, respectively (Figure S1). This indicates that **1** exists as a monomer in solution state, which is also reflected in the solid-state structure. MS analysis gave a molecular ion at 500 *m/z*, confirming its identity. Compound **1** was found to be highly volatile and sublimed at 80 °C (0.5 mbar) with no visible solid remaining. Thermogravimetric analysis (TGA) showed the new precursor volatilized completely in a single step from 145 to 215 °C, with only 2% of residual mass (Figure 2). A thermal stress test with a higher mass loading of precursor showed a slight shift to a higher temperature (160−235 °C) without signs of decomposition (Figure S3a). The 1 Torr vapor pressure of **1** was shown to occur at 134 °C (Figure S3b), and its Δ*H* of vaporization was 65.8 kJ mol^{-1} (Figure S3c).
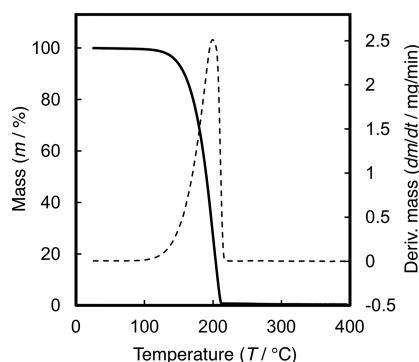
Figure 2. Thermogravimetric analysis of compound **1**.

The heterolytic bond dissociation energy of the In−N bonds for **1** was calculated by density functional theory (DFT) to be 289 kJ mol^{-1}, which is lower than that of In(famd)$_3$ (312 kJ mol^{-1}) (Table S6) and indicates a slightly weaker In−N bond. The natural charges of the In (+1.47) and N (−0.44) atoms of **1** show a less polarized In−N bond character in comparison to the previously used In(famd)$_3$ (In, +1.78; N, −0.69) (Table S7). Both the HOMO π and LUMO π^* frontier orbitals of **1** are localized on the N$_3$ moiety of the triazenide ligand (Figure 3a,b). The high electron density on the backbone of the ligand
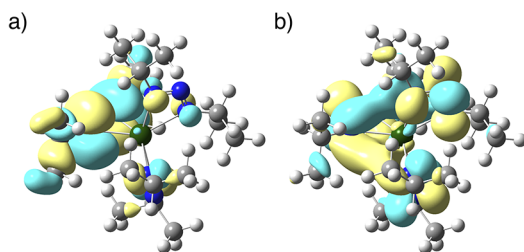

Figure 3. (a) HOMO (−5.90 eV) and (b) LUMO (−0.69 eV) of **1** from DFT calculations.

could explain the increased volatility of **1** due to electrostatic repulsion forces in solid state. This is consistent with the crystal structure, which is highly disordered because of a lack of intermolecular interactions.

2.2. ALD of InN Using In(III) Triazenide Precursor. ALD of InN was tested initially on Si(100) using 5 s pulse of **1** and 9 s NH$_3$ plasma pulse, separated by a 9 s N$_2$ purge, while varying the deposition temperature. These experiments revealed two temperature intervals where the growth per cycle (GPC) was constant with temperature, at 220−250 °C and 300−350 °C (Figure 4a). Saturation curves on Si(100) of the lower and higher temperature intervals showed saturation growth behavior with a GPC of 0.4 Å/cycle and 1.2 Å/cycle, respectively, after a 5 s pulse of **1** and 9 s pulse of NH$_3$ plasma (Figure 4b,c). These results indicate a self-limiting surface chemistry for **1** and NH$_3$ plasma at both the lower and higher temperature regions. The high-temperature interval growth rate is three and four times that of our previous reports using In(famd)$_3$ (0.4 Å/cycle)[23] and InMe$_3$ (0.32 Å/cycle)[10], respectively, with NH$_3$ plasma.

Furthermore, the high-temperature interval indicates a higher thermal stability of the chemisorbed species in comparison to the previously used In(famd)$_3$, which has a constant GPC over a wide temperature range of 200−280

°C.[23] A linear growth trend was observed when all the parameters were kept constant upon increasing ALD cycles at 220 and 300 °C (Figures S7 and 4d).

2.3. Thermal Properties of In(III) Triazenide Precursor. The presence of two temperature intervals with self-limiting growth is highly exceptional for ALD. Differential scanning calorimetry (DSC) analysis of **1** shows two exothermic events, a sharp peak between 150 and 180 °C, and a broad peak between 220 and 280 °C (Figure S4). The onset temperature of the first exothermic event coincides with the onset volatilization temperature observed in the TGA (∼145 °C), which could indicate decomposition and volatilization occurring simultaneously. Heating of **1** in solid state to 180 °C for 16 h showed only slight discoloration of the sample with no signs of decomposition by ^{1}H NMR analysis. These results suggest that the first exothermic event does not correspond to a decomposition pathway. The spike in growth rate between 250 and 300 °C lines up with the second broad exothermic event between 220 and 280 °C, which contains three overlapping peaks at approximately 245, 255, and 270 °C. Heating studies of **1** in solid and solution states (Figure S5) above 200 °C confirmed this to be a decomposition event, giving In metal and an unidentifiable brown solid. This is a strong indication that **1** decomposes in the gas-phase inside the deposition chamber to a more volatile and reactive species at ∼250 °C. It is worth pointing out that even though this is usually an unwanted ALD precursor property, in this case the decomposition product still retains self-limiting growth behavior.

The thermal decomposition of **1** was studied by DFT calculations at 300 °C showing two possible pathways (Figure 5a). The first common step of both pathways is a transfer of a hydrogen from the methyl group of the isopropyl moiety to the endocyclic nitrogen, releasing a propene molecule to form **A**. Compound **A** can tautomerize through a hydrogen transfer to the exocyclic nitrogen to give **B**. The other possible path, which is more energetically favored, is migration of the hydrogen onto the exocyclic tertiary nitrogen while simultaneously releasing N$_2$ to form **C**. The free energies for the decomposition path are shown at 300 °C (Figure 5b). The energy for the final structure **C** ($\Delta G° = -245$ kJ mol^{-1}) is much lower than **1** due to the large increase of entropy when releasing two molecules. This indicates that at higher temperature and lower pressure, structure **C** would be expected to dominate. Further calculations show that all three ligands decompose simultaneously via this pathway to give a tricoordinated In(III) species of **C** (Tables S10 and S11). Decomposition of the triazenide ligand of **1** is uniquely different to that of amidinates and guanidinates, which have been shown to thermally decompose by either carbodiimide deinsertion or β-hydrogen abstraction.[41] This highlights the reduced hydride reactivity of the β-hydrogen on the isopropyl moiety by the electron-withdrawing triazenide ligand and removes the need for a bulky *tert*-butyl exocyclic substituent to block this position.

2.4. InN Film Characterization. The films deposited at both temperature intervals rendered polycrystalline hexagonal wurtzite InN on Si(100) (Figure S8a−c). Deposition on 4H-SiC(0001), which has a smaller lattice mismatch with InN,[3] at 325 °C with 5 s pulse of **1** and 9 s NH$_3$ plasma pulse rendered epitaxial wurtzite InN. The θ-2θ X-ray diffraction (XRD) measurement shows InN peaks corresponding to the (0002), (0004), and (0006) planes indicating growth along the *c*-axis
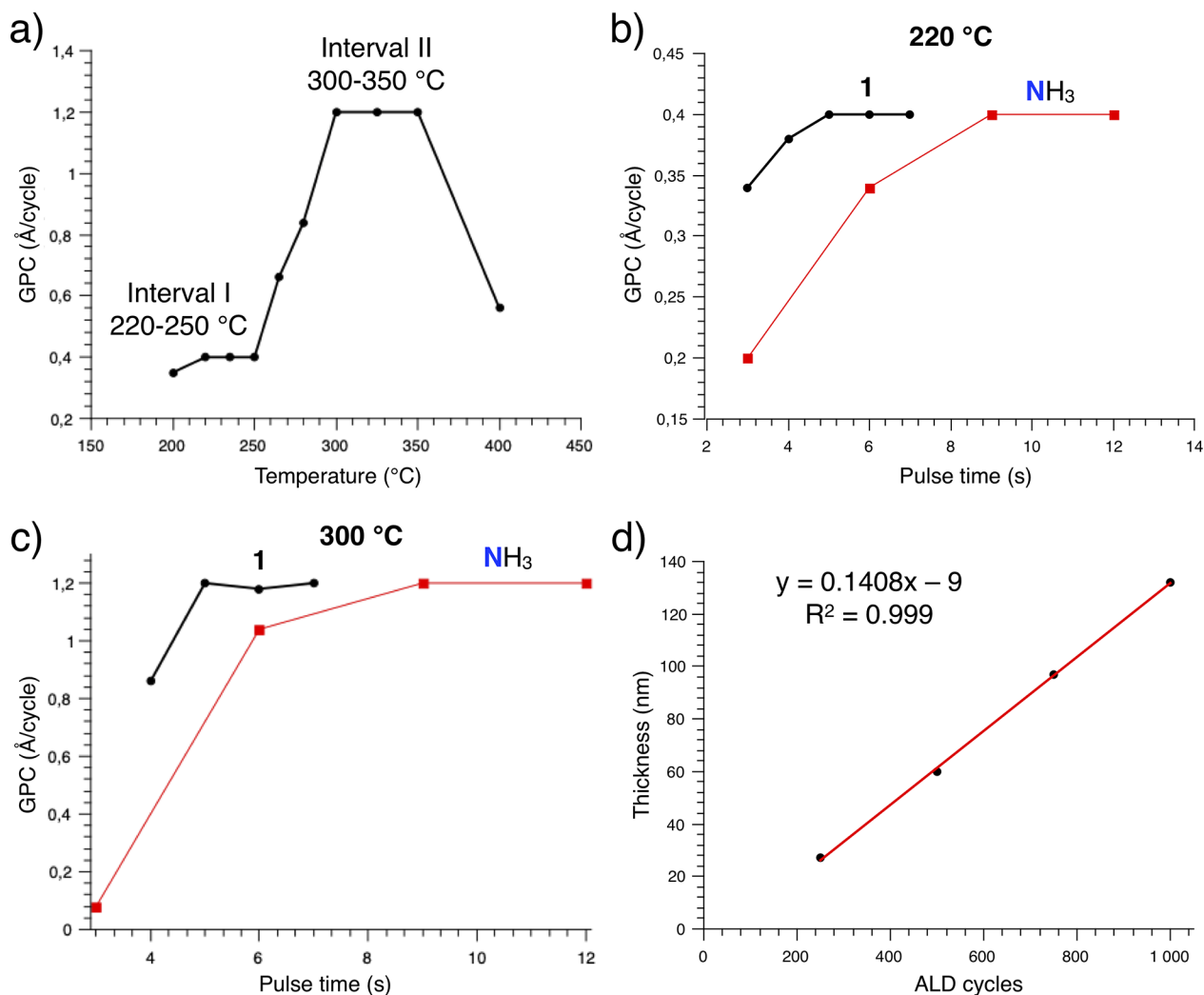
Figure 4. (a) Growth dependence on process temperature using a 5 s pulse of **1** and 9 s pulse of NH_3 on Si(100). (b) Growth per cycle behavior of **1** and NH_3 pulses deposited at 220 °C on Si(100). (c) Growth per cycle behavior of **1** and NH_3 pulses deposited at 300 °C on Si(100). (d) Growth behavior of **1** at 300 °C dependent on the number of cycles using a 5 s pulse of **1** and a 9 s NH_3 plasma pulse on Si(100). The red line indicates the linear trend.

(Figure 6a). Grazing incidence XRD (GIXRD) shows no peaks, indicating no tilted grains (Figure S8d). XRD pole figures of the InN(10−11) and (10−12) peaks were constructed to study the in-plane grain orientation and the crystal relationship between the film and the substrate (Figures S9 and 6b). Both pole figures show 12 poles, with 6 poles corresponding to 4H-SiC(hkil) and 6 poles to the InN film. This is expected for an epitaxially grown hexagonal film on a hexagonal substrate due to its six-folded symmetry. Note that in the (10−11) plane (Figure S9), the poles for the substrate and the InN film overlap. A distinct difference between the substrate and the InN poles was observed for the (10−12) plane (Figure 6b), where the inner 6 poles correspond to the InN film, and the outer 6 poles correspond to the SiC substrate.

The θ-2θ XRD, GIXRD, and pole figure measurements show that each InN hexagon grows epitaxially on a SiC hexagon, with in-plane relations InN [10−11] ∥ 4H-SiC [10−11] and InN [10−12] ∥ 4H-SiC [10−12]. This confirms the epitaxial relationship between the InN film and the SiC substrate along the c-axis; InN [0002] ∥ 4H-SiC [0001].

A top-view scanning electron microscope (SEM) image of the InN films on 4H-SiC shows homogeneously ordered grains along horizontal lines with a line width of approximately 130 nm (Figure 6c). This indicates that the InN films grow on the terrace of the 4H-SiC substrate, leaving partially uncoated step-edges.[42] We speculate that the step-edge acts as a surface diffusion barrier for the atoms, forcing them to nucleate at the step-edge, and the InN film starts to grow along the terrace. The species on the terrace have a higher surface diffusion compared to the species on the step allowing them to move toward the steps to nucleate.[42,43] X-ray photoelectron spectroscopy (XPS) of the film deposited on 4H-SiC at 325 °C with 5 s pulse of **1** and 9 s NH_3 plasma pulse showed 48.7 ± 2.4 at. % In, 48.6 ± 2.4 at. % N, 2.7 ± 0.1 at. % O and no detectable C (Figure S12). The same amount of oxygen is bonded to In and N, giving perfect In/N ratio of 1.0. It should be noted that the InN film was capped with approximately 10 nm of AlN to avoid post deposition oxidation of the InN film. As preferential sputtering of InN can occur, this was minimized by applying the lowest sputtering energy and no tilting of the sample according to previously reported protocols.[44] The high-
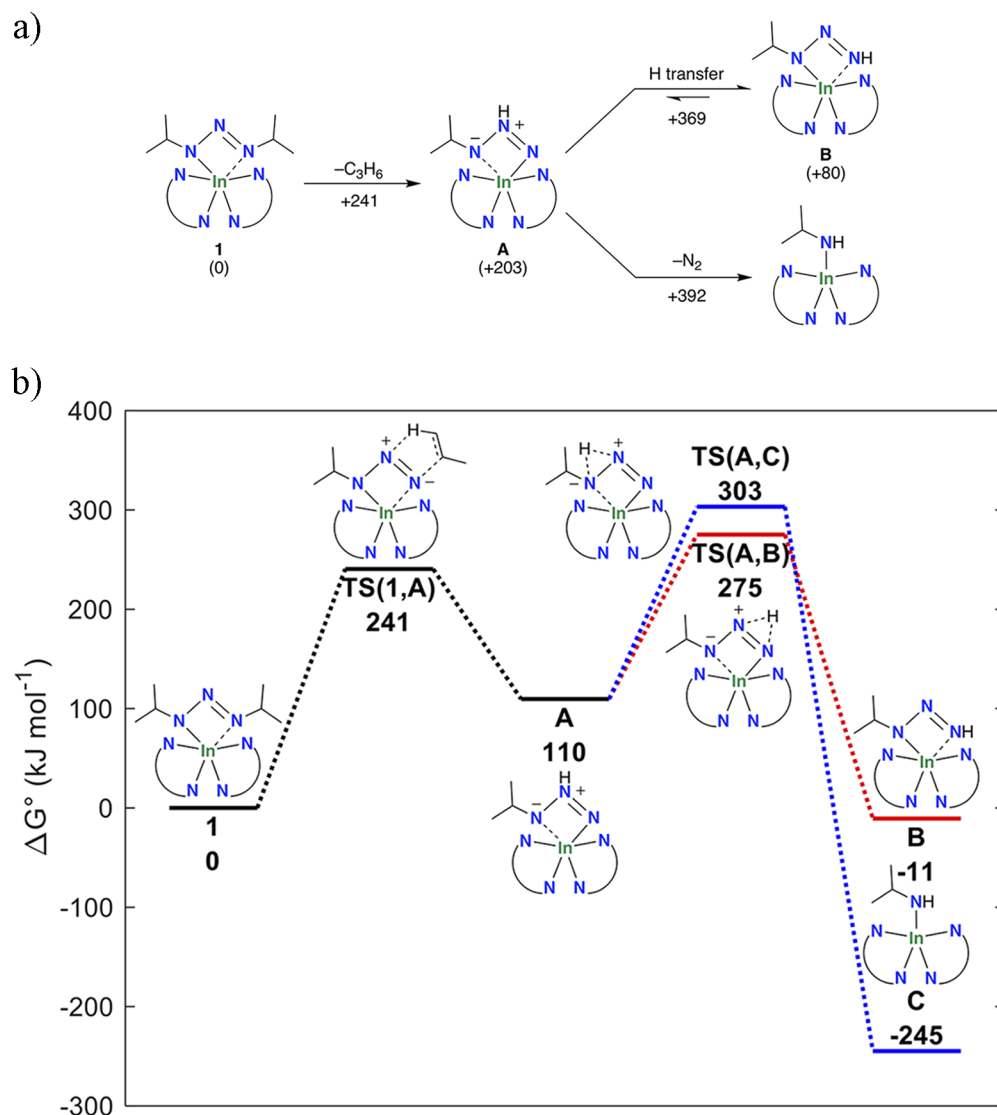
a)

b)

Figure 5. (a) DFT calculated decomposition pathways for the thermal decomposition of **1** at 300 °C. The change in enthalpy is shown in each step and is given in kJ mol^{-1}. (b) Free energy profile for the decomposition of **1** at 300 °C. The free energies are marked for each pathway and are given in kJ mol^{-1}.

resolution XPS of In 3d$_{5/2}$ and N 1s was fitted with two subpeaks each. For In 3d$_{5/2}$, the major contribution at 444.6 eV was assigned to the In−N bond, with a minor contribution at 445.7 eV assigned to the In−O bond. For the N 1s, the major contribution at 396.5 eV was assigned to the N−In bond, with a minor contribution at 397.6 eV assigned to the N−O bond.[45−47] Raman spectroscopy of the InN films on 4H-SiC deposited at 325 °C (Figure 6d) shows the A$_1$(LO) band of wurtzite InN at approximately 573 cm^{-1}, which agrees well with previously reported Raman shift[48] and indicates low stress in the film. A very small shoulder was observed at 375 cm^{-1}, which is a gap mode previously shown to correspond to In vacancies in InN.[48] The appearance of this gap mode is attributed to the small amount of oxygen in the film. The sheet resistance of 50 nm InN films is on average 920 Ω/sq, which corresponds to a resistivity of 0.46 Ω cm. This value is comparable to previously reported InN deposited by ALD at 240 °C.[8] We could not determine the carrier concentration and the carrier mobility with high accuracy due to the limitations of the instrument used. The fitted electron mobility

values are 10−500 cm^2/(V s) depending on its correlated carrier concentration. We believe that this scattering is due to the confidence level of the fitting. Assuming a carrier concentration of 1×10^{20} cm^{-3}, the mobility is approximately 13 cm^2/(V s). This value is in the same range as previously reported for InN films from ALD deposited at somewhat lower temperature.[8]

3. CONCLUSIONS

In conclusion, we have developed a new highly volatile In(III) precursor and shown for the first time the use of a homoleptic triazenide in a vapor deposition process. This compound was easily synthesized using cheap and easily obtainable reagents. Thermogravimetric analysis showed that **1** underwent single step volatilization between 145 and 215 °C with negligible mass remaining, and heating studies showed it started to slowly decomposed at ∼200 °C. Interestingly, **1** undergoes decomposition in the gas-phase at higher deposition temperatures to give a more reactive In(III) compound that still
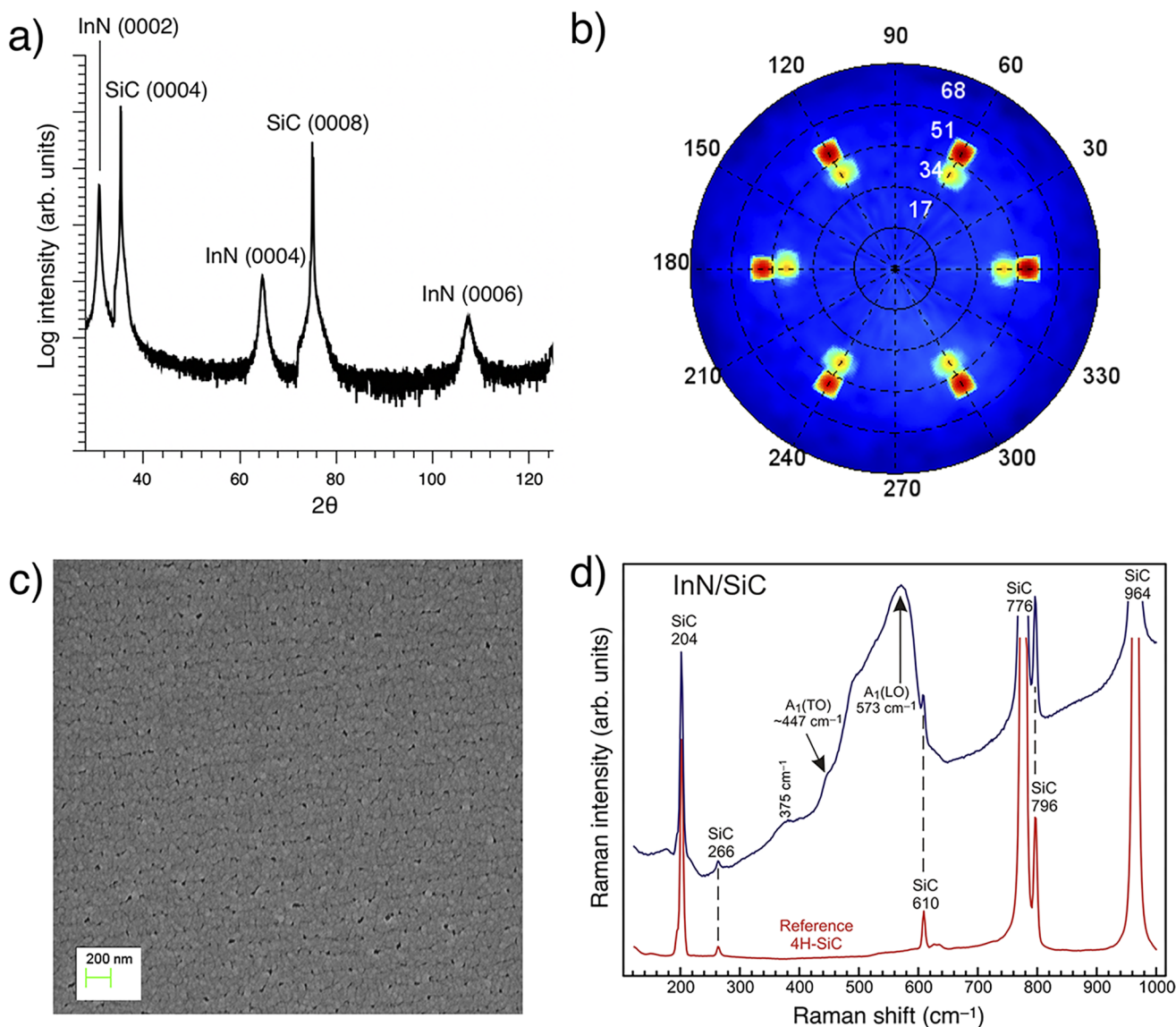
Figure 6. (a) XRD of InN on 4H-SiC(0001) using a 5 s pulse of **1** and 9 s NH$_3$ plasma pulse deposited at 325 °C showing epitaxial InN along the *c*-axis. (b) Pole figure of the InN(10−12) plane showing 12 poles, the outer 6 red poles corresponding to SiC and the inner 6 green/yellow poles to InN. (c) Top view SEM of InN on 4H-SiC deposited at 325 °C. (d) Raman spectrum of InN on 4H-SiC deposited at 325 °C together with the reference spectrum of the substrate provided for comparison. The lines belonging to the SiC substrate are labeled "SiC" with their corresponding Raman shifts in cm^{-1}.

possesses self-limiting behavior and without unwanted impurities in the film. DFT calculations showed that **1** decomposes to a smaller tricoordinated In(III) compound by liberating three molecules of propene and N$_2$, and explains the increased growth rate observed in the higher temperature interval. This result has the potential to open a new path in ligand and precursor design for vapor deposition with deliberate gas-phase decomposition. ALD of InN using **1** and NH$_3$ plasma afforded epitaxial InN on 4H-SiC that was stoichiometric and with a very low level of impurities. Initial electrical characterization of the InN films shows a sheet resistivity of 920 Ω/sq and electron mobility on par with the reported literature. This new triazenide ligand has potential to unlock ALD of InN for semiconductor applications and develop a new class of M−N bonded precursors for future ALD processes.

4. EXPERIMENTAL SECTION

4.1. General Experimental Procedures. *Caution! As catenated nitrogen compounds are known to be associated with explosive hazards, isopropylazide and compound* **1** *are possible explosive energetic materials. Although we have not experienced any problems in the synthesis, characterization, sublimation, and handling of compound* **1**, *its energetic properties have not been investigated and are therefore unknown. We therefore highly recommend all appropriate standard safety precautions for handling explosive materials (safety glasses, face shield, blast shield, leather gloves, polymer apron, and ear protection) be used at all times when working with isopropylazide and compound* **1**. All reactions and manipulations were carried out under an N$_2$ atmosphere; on a Schlenk line using Schlenk air-free techniques and in a GS Glovebox-Systemtechnik glovebox. All anhydrous solvents were purchased from Sigma-Aldrich and further dried with 4 Å molecular sieves. InCl$_3$ (98%) and isopropyllithium solution were purchased from Sigma-Aldrich and both used without further purification. Isopropylazide was synthesized according to the literature procedure.[40] All NMR spectra

were measured with an Oxford Varian 300 MHz spectrometer. The C_6D_6 solvent peaks were used as an internal standard for the ^1H NMR (300 MHz) and $^{13}C\{^1H\}$ NMR (75 MHz) spectra. The electrospray ionization (ESI)-MS data was obtained on a Thermo Scientific LCQ Fleet ESI-MS instrument. The melting point was determined in a capillary sealed under N_2 with a Stuart SMP10 melting point apparatus and is uncorrected. Elemental analysis was performed by Mikroanalytisches Laboratorium Kolbe, Germany.

4.2. Synthesis of Tris(1,3-diisopropyltriazenide)indium(III) (1). To a solution of isopropylazide[40] (5.90 g, 69.3 mmol) in Et_2O (100 mL) at −78 °C was added isopropyllithium (0.7 M in pentane, 99.0 mL, 69.3 mmol). The reaction mixture was stirred for 30 min and then allowed to warm up to room temperature for 1 h. This solution was then added to a −78 °C solution of $InCl_3$ (5.11 g, 23.1 mmol) in THF (100 mL) via cannula and the mixture was stirred at this temperature for 20 min. The reaction was warmed to room temperature and stirred for 16 h. The reaction mixture was concentrated under reduced pressure, and the resulting residue was dissolved in *n*-hexanes, filtered through a pad of Celite, and concentrated under reduced pressure to give a light-yellow solid. The solid was purified by sublimation at 80 °C (0.5 mbar) to give compound **1** as a solid (8.19 g, 71%).

1: Colorless solid, decomp. 212−214 °C. ^1H NMR (300 MHz, C_6D_6) δ 1.23 (d, J = 6.0 Hz, 36H, CH_3), 4.06 (sept, J = 6.0 Hz, 6H, CH). $^{13}C\{^1H\}$ NMR (75 MHz, C_6D_6) δ 24.0 (s, CH_3), 53.7 (s, CH). LRMS (ESI, positive) m/z = 500 $[M + H]^+$. Anal. calcd. for $C_{18}H_{42}InN_9$: C, 43.29%; H, 8.48%; N, 25.24%. Found: C, 42.64%; H, 8.25%; N, 24.90%.

4.3. X-ray Crystallographic Analysis. Colorless single crystals were obtained by recrystallization from *n*-hexanes at −35 °C for **1**. The single crystals were used for X-ray diffraction data collection on a Bruker D8 SMART Apex-II diffractometer using graphite-mono-chromated Mo−Kα radiation (λ = 0.71073 Å). All data were collected in hemisphere with over 95% completeness to $2\theta < 50.05°$. The structures were solved by direct methods. The coordinates of metal atoms were determined from the initial solutions, and of the N and C methods, located in subsequent differential Fourier syntheses. All non-hydrogen atoms were refined first in isotropic and then in anisotropic approximation using Bruker SHELXTL software. Additional crystal data are available at the Cambridge Crystallographic Data Centre, deposition no. CCDC 1966432.

4.4. Thermogravimetric Analysis. Volatilization and vapor pressure curves were collected using a TA Instruments thermogravi-metric analysis Q500 tool inside an N_2 filled glovebox. The ramp experiment of **1** was undertaken in tared platinum pans loaded with 6 mg and 17 mg of **1** for low and high mass volatilization experiments, respectively. The furnace was heated at a rate of 10 °C/min to 500 °C with a maintained N_2 flow rate of 60 sccm.

4.5. Differential Scanning Calorimetry Analysis. The DSC measurement for **1** was performed on a TA Instruments DSC Q10 tool. A sample of ∼0.2 mg of **1** was prepared in a sealed aluminum pan in an N_2 filled glovebox. The sample of **1** and a blank reference pan was heated at a rate of 10 °C/min to 400 °C.

4.6. Quantum-Chemical Computations. All quantum chemical computations were preformed using Gaussian 16 software.[49] Structural optimization and harmonic normal mode vibrational calculations were undertaken using the hybrid DFT method B3LYP[50,51] together with Grimme's version 3 dispersion correction[52] and def2TZVP[53,54] basis set. The decomposition path was investigated by searching for possible stable structures as well as finding transition states connecting these structures. Minima were confirmed to have no imaginary frequencies, while transition states were verified to have one imaginary frequency, lying along the reaction path.

4.7. Film Deposition. A hot-wall Picosun R-200 was used for the deposition of InN, which was equipped with a Litmas remote plasma source. The tool operated at 4 mbar with a continuous flow of high purity N_2 (99.999%) into the chamber, which was also used as the purge gas. The system was equipped with a traditional stainless-steel precursor container (bubbler), albeit without dip-tube for the

incoming carrier gas. The system was baked at 450 °C for 2 h with a 300 sccm flow of N_2 to remove traces of H_2O and O_2 in the deposition chamber after exposure to the atmosphere during substrate exchange. In an N_2 filled glovebox, ∼300 mg of **1** was weighed into a glass vial, which was placed in a stainless-steel container and assembled onto the ALD tool. *Caution! The bubbler must not be overfilled with multigram scale of precursor **1** due to possible explosion risk.* The optimal temperature for the bubbler to obtain a high enough vapor pressure to saturate the substrate surface and obtain optimal growth was 125 °C. An amount of ∼300 mg of precursor was enough for 500 cycles, and increased linearly with the number of cycles. NH_3 plasma was used as the nitrogen source, containing a 100/75 sccm Ar/NH_3 gas mixture with a 2800 W plasma power and was located approximately 75 cm above the substrate.[10] Unless otherwise stated, a 9 s NH_3 pulse was used followed by a 10 s purge. The Si(100) and 4H-SiC substrates were cut into 15 × 15 mm^2 pieces, and films were deposited onto them without any further *ex situ* cleaning. Prior to deposition, a 120 s pulse of H_2 plasma (1000 W, gas mixture of Ar/H_2 100/10 sccm) and N_2 plasma (2800 W, gas mixture of Ar/N_2 80/380 sccm) was employed to nitridize the substrate surface and to remove residual H_2O and O_2 from inside the deposition chamber.

4.8. Film Characterization. Film thickness and film crystallinity (θ-2θ) were measured with X-ray reflectivity (XRR), PANalytical X'Pert PRO with a Cu-anode tube and Bragg−Brentano HD optics. To analyze the thickness, the software PANalytical X'Pert reflectivity and a two-layer model was used to fit the data, InN/substrate. PANalytical EMPYREAN MRD XRD with a Cu-anode X-ray tube and 5-axis (x-y-z-v-u) sample stage operating at 45 kV and 40 mA was used in GIXRD mode with 0.5° incident angle to analyze the crystallinity of the films. The pole figures were obtained with the same XRD equipment and operating parameters using an X-ray lens and parallel plate collimator. The morphology of the films was examined with a LEO 1550 SEM operating at an acceleration energy of 10 kV. Kratos AXIS Ultra DLD XPS was used to analyze the composition and the chemical environment of the atoms in the film. The XPS tool was equipped with an Ar sputtering source (0.5 keV), which was used for clean sputtering and depth profiling of the films. To analyze the data, CasaXPS was used. The high-resolution scans were fitted by Gaussian-Laurentius functions and Shirley background. Raman spectra were recorded on a micro-Raman setup utilizing 100× objective and 532 nm solid-state laser (Coherent, Sapphire SF 532−150). The laser was focused to a ∼0.8 μm spot on the sample and a power below 1 mW was used to avoid overheating. The Raman signal was dispersed by a monochromator (Jobin Yvon, HR460) coupled to a CCD camera. With the 600 grooves/mm grating used in this measurement, the resolution was about 5.5 cm^{-1}. To obtain high signal-to-noise ratio, 100 subsequent acquisitions of 10 s were obtained for each sample resulting in a total acquisition time of 1000 s. No changes were observed in the spectra during the series, indicating that the laser power utilized was sufficiently low to avoid thermal damage.

■ ASSOCIATED CONTENT

Ⓢ Supporting Information

The Supporting Information is available free of charge at https://pubs.acs.org/doi/10.1021/acs.chemmater.9b05171.

Precursor and film characterization, and computational calculations data (PDF)

Crystallographic data (CIF)

■ AUTHOR INFORMATION

Corresponding Author

Nathan J. O'Brien − *Department of Physics, Chemistry and Biology, Linköping University, Linköping SE-58183, Sweden;* Ⓞ orcid.org/0000-0003-3633-9674; Email: nathan.o.brien@liu.se

Authors

Polla Rouf − *Department of Physics, Chemistry and Biology, Linköping University, Linköping SE-58183, Sweden;*
 ⓘ orcid.org/0000-0002-1452-4548

Rouzbeh Samii − *Department of Physics, Chemistry and Biology, Linköping University, Linköping SE-58183, Sweden*

Karl Rönnby − *Department of Physics, Chemistry and Biology, Linköping University, Linköping SE-58183, Sweden;*
 ⓘ orcid.org/0000-0002-8066-9454

Sydney C. Buttera − *Department of Chemistry, Carleton University, Ottawa, Ontario K1S 5B6, Canada*

Chih-Wei Hsu − *Department of Physics, Chemistry and Biology, Linköping University, Linköping SE-58183, Sweden*

Ivan G. Ivanov − *Department of Physics, Chemistry and Biology, Linköping University, Linköping SE-58183, Sweden*

Vadim Kessler − *Department of Molecular Sciences, Swedish University of Agricultural Sciences, 75007 Uppsala, Sweden*

Lars Ojamäe − *Department of Physics, Chemistry and Biology, Linköping University, Linköping SE-58183, Sweden;*
 ⓘ orcid.org/0000-0002-5341-2637

Henrik Pedersen − *Department of Physics, Chemistry and Biology, Linköping University, Linköping SE-58183, Sweden;*
 ⓘ orcid.org/0000-0002-7171-5383

Complete contact information is available at:
https://pubs.acs.org/10.1021/acs.chemmater.9b05171

Notes

The authors declare no competing financial interest.

■ REFERENCES

(1) Bhuiyan, A. G.; Hashimoto, A.; Yamamoto, A. Indium Nitride (InN): A Review on Growth, Characterization and Properties. *J. Appl. Phys.* **2003**, *94*, 2779−2808.

(2) Butcher, K. S. A.; Tansley, T. L. Latest Development and a Review of the Band-Gap Controversy. *Superlattices Microstruct.* **2005**, *38*, 1−37.

(3) Zhang, B. L.; Sun, G. S.; Guo, Y.; Zhang, P. F.; Zhang, R. Q.; Fan, H. B.; Liu, X. L.; Yang, S. Y.; Zhu, Q. S.; Wang, Z. G. Valence band offset of InN/4H-SiC heterojunction measured by x-ray photoelectron spectroscopy. *Appl. Phys. Lett.* **2008**, *93*, 242107.

(4) Ivanov, S. V.; Shubina, T. V.; Komissarova, T. A.; Jmerik, V. N. Metastable Nature of InN and In-Rich InGaN Alloys. *J. Cryst. Growth* **2014**, *403*, 83−89.

(5) Ruffenach, S.; Moret, M.; Briot, O.; Gil, B. Recent Advances in the MOVPE Growth of Indium Nitride. *Phys. Status Solidi A* **2010**, *1*, 9−18.

(6) Zhou, J.; Huang, Q.; Li, J.; Cai, D.; Kang, J. The InN Epitaxy via Controlling In Bilayer. *Nanoscale Res. Lett.* **2014**, *9*, 5.

(7) George, S. M. Atomic Layer Deposition: An Overview. *Chem. Rev.* **2010**, *110*, 111−131.

(8) Nepal, N.; Mahadik, N. A.; Nyakiti, L. O.; Qadri, S. B.; Mehl, M. J.; Hite, J. K.; Eddy, C. R. J. Epitaxial Growth of Cubic and Hexagonal InN Thin Films via Plasma-Assisted Atomic Layer Epitaxy. *Cryst. Growth Des.* **2013**, *13*, 1485−1490.

(9) Haider, A.; Kizir, S.; Biyikli, N. Low-Temperature Self-Limiting Atomic Layer Deposition of Wurtzite InN on Si(100). *AIP Adv.* **2016**, *6*, 045203.

(10) Deminskyi, P.; Rouf, P.; Ivanov, I. G.; Pedersen, H. Atomic Layer Deposition of InN Using Trimethylindium and Ammonia Plasma. *J. Vac. Sci. Technol., A* **2019**, *37*, 020926.

(11) Wakahara, A.; Tsuchiya, T.; Yoshida, A. Epitaxial Growth of Indium Nitride. *J. Cryst. Growth* **1990**, *99*, 385−389.

(12) Feng, X.; Peng, H.; Gong, J.; Wang, W.; Liu, H.; Quan, Z.; Pan, S.; Wang, L. Epitaxial Growth of InN Thin Films by Plasma-Enhanced Atomic Layer Deposition. *J. Appl. Phys.* **2018**, *124*, 243104.

(13) Bürger, H.; Cichon, J.; Goetze, U.; Wannagat, U.; Wismar, H. Beiträgezur Chemie Der Silicium-Stickstoff-Verbindungen: CVII. Darstellung, Schwingungsspektren Und Normalkoordinatenanalyse von Disilylamiden Der 3. Gruppe: $M[N(SiMe_3)_2]_3$ Mit M = Al, Ga Und In. *J. Organomet. Chem.* **1971**, *33*, 1−12.

(14) Rossetto, G.; Brianese, N.; Camporese, A.; Porchia, M.; Zanella, P.; Bertoncello, R. Synthesis and Charaeterization of Hexakis-(Diethylamido)Diindium(III) and Bis-Cyclopentadienyl-(Diethylamido)Indium(III). *Main Gr. Met. Chem.* **1991**, *14*, 113−122.

(15) Petrie, M. A.; Ruhlandt-Senge, K.; Hope, H.; Power, P. P. Structural Studies of the Monomeric, Low Coordinate, Indium Amides (t-Bu)$_2$InN(2,6-i-Pr$_2$C$_6$H$_3$)SiPh$_3$ and In{N(SiMe$_3$)$_2$}$_3$. *Bull. Soc. Chim. Fr.* **1993**, *130*, 851−855.

(16) Frey, R.; Gupta, V. D.; Linti, G. Monomere Bis- Und Tris(Amide) Des Indiums. *Z. Anorg. Allg. Chem.* **1996**, *622*, 1060−1064.

(17) Kim, J.; Bott, S. G.; Hoffman, D. M. Synthesis of Indium Amide Compounds. *Inorg. Chem.* **1998**, *37*, 3835−3841.

(18) Gebhard, M.; Hellwig, M.; Kroll, A.; Rogalla, D.; Winter, M.; Mallick, B.; Ludwig, A.; Wiesing, M.; Wieck, A. D.; Grundmeir, G.; et al. New Amidinate Complexes of Indium(III): Promising CVD Precursor for Transparent and Conductive In$_2$O$_3$ Thin Films. *Dalt. Trans.* **2017**, *46*, 10220−10231.

(19) Kim, S. B.; Jayaraman, A.; Chua, D.; Davis, L. M.; Zheng, S.-L.; Zhao, X.; Lee, S.; Gordon, R. G. Obtaining a Low and Wide Atomic Layer Deposition Window (150−275 °C) for In$_2$O$_3$ Films Using an InIII Amidinate and H$_2$O. *Chem. - Eur. J.* **2018**, *24*, 9525−9529.

(20) Barry, S. T.; Gordon, P. G.; Ward, M. J.; Heikkila, M. J.; Monillas, W. H.; Yap, G. P. A.; Ritala, M.; Leskelä, M. Chemical Vapour Deposition of In2O3 Thin Films from a Tris-Guanidinate Indium Precursor. *Dalt. Trans.* **2011**, *40*, 9425−9430.

(21) Gebhard, M.; Hellwig, M.; Parala, H.; Xu, K.; Winter, M.; Devi, A. Indium-Tris-Guanidinates: A Promising Class of Precursors for Water Assisted Atomic Layer Deposition of In$_2$O$_3$ Thin Films. *Dalt. Trans.* **2014**, *43*, 937−940.

(22) McCarthy, R. F.; Weimer, M. S.; Emery, J. D.; Hock, A. S.; Martinson, A. B. F. Oxygen-Free Atomic Layer Deposition of Indium Sulfide. *ACS Appl. Mater. Interfaces* **2014**, *6*, 12137−12145.

(23) Rouf, P.; O'Brien, N. J.; Rönnby, K.; Samii, R.; Ivanov, I. G.; Ojamäe, L.; Pedersen, H. The Endocyclic Carbon Substituent of Guanidinate and Amidinate Precursors Controlling ALD of InN Films. *J. Phys. Chem. C* **2019**, *123*, 25691−25700.

(24) Gantzel, P.; Walsh, P. J. Synthesis and Crystal Structures of Lithium and Potassium Triazenide Complexes. *Inorg. Chem.* **1998**, *37*, 3450−3451.

(25) Nimitsiriwat, N.; Gibson, V. C.; Marshall, E. L.; Takolpuckdee, P.; Tomov, A. K.; White, A. J. P.; Williams, D. J.; Elsegood, M. R.; Dale, S. H. Mono- versus Bis-Chelate Formation in Triazenide and Amidinate Complexes of Magnesium and Zinc. *Inorg. Chem.* **2007**, *46*, 9988−9997.

(26) Dwyer, F. P. Chelation in Metallic Triazene Salts. *J. Am. Chem. Soc.* **1941**, *63*, 78−81.

(27) Corbett, M.; Hoskins, B. F. The Structure of Monoclinic Tris(l,3-Diphenyltriazenato)Cobalt(III)- Toluene (1/1): An Octahedral Complex Containing Three Four-Membered Chelate Rings. *Aust. J. Chem.* **1974**, *27*, 665−670.

(28) Black, D. S. C.; Davis, V. C.; Deacon, G. B.; Schultze, R. J. Tris(Triazenido)Thallium(III) Compounds. *Inorg. Chim. Acta* **1979**, *37*, L528.

(29) Guzei, I. A.; Liable-Sands, L. M.; Rheingold, A. L.; Winter, C. H. Synthesis and Characterization of Titanium and Zirconium Complexes Bearing Diphenyltriazenido Ligands. *Polyhedron* **1997**, *16*, 4017−4022.

(30) Ríos-Moreno, G.; Aguirre, G.; Parra-Hake, M.; Walsh, P. J. Synthesis, Characterization, and Structure of Dinuclear Copper(I) and Silver(I) Complexes of Ortho-Functionalized 1,3-Bis(Aryl)-Triazenide Ligands. *Polyhedron* **2003**, *22*, 563.

(31) Johnson, A. L.; Willcocks, A. M.; Richards, S. P. Synthesis and Structures of Group 11 Metal Triazenide Complexes: Ligand Supported Metallophilic Interactions. *Inorg. Chem.* **2009**, *48*, 8613−8622.

(32) Lee, H. S.; Niemeyer, M. Homoleptic Heavy Alkaline Earth and Europium Triazenides. *Inorg. Chem.* **2010**, *49*, 730−735.

(33) Hinz, A.; Schulz, A.; Villinger, A.; Wolter, J.-W. Cyclo-Pnicta-Triazanes: Biradicaloids or Zwitterions? *J. Am. Chem. Soc.* **2015**, *137*, 3975−3980.

(34) Flanagan, K. R.; Parish, J. D.; Fox, M. A.; Johnson, A. L. Synthetic, Structural, and Computational Studies on Heavier Tetragen and Chalcogen Triazenide Complexes. *Inorg. Chem.* **2019**, *58*, 16660−16666.

(35) Leman, J. T.; Barron, A. R.; et al. Synthesis of 1,3-Diphenyltriazenide Complexes of Aluminium, Gallium and Indium: Crystal Structure of Tris(1,3-Diphenyltriazenido)Aluminium(III). *Polyhedron* **1989**, *8*, 1909−1912.

(36) Leman, J. T.; Roman, H. A.; Barron, A. R. Five- and Six-Coordinate Organometallic Compounds of Indium. *Organometallics* **1993**, *12*, 2986−2990.

(37) Brinckman, F. E.; Haiss, H. S.; Robb, R. A. Metal-Nitrogen Bonding. Covalent Complexes of 1,3-Dimethyltriazene with Elements of Groups I, II, III, IV, and V. *Inorg. Chem.* **1965**, *4*, 936−942.

(38) Soussi, K.; Mishra, S.; Jeanneau, E.; Millet, J.-M.; Daniele, S. Asymmetrically Substituted Triazenes as Poor Electron Donor Ligands in the Precursor Chemistry of Iron(II) for Iron-Based Metallic and Intermetallic Nanocrystals. *Dalt. Trans.* **2017**, *46*, 13055−13064.

(39) Soussi, K.; Mishra, S.; Jeanneau, E.; Mantoux, A.; Stéphane, D. Synthesis, Characterization and Thermal Transport Properties of Heteroleptic N-alkyltriazenide Complexes of Titanium(IV) and Niobium(V). *Polyhedron* **2018**, *152*, 84−89.

(40) Swetha, M.; Venkata Ramana, P.; Shirodkar, S. G. Simple and Efficient Method for the Synthesis of Azides in Water-THF Solvent System. *Org. Prep. Proced. Int.* **2011**, *43*, 348−353.

(41) Barry, S. T. Amidinates, Guanidinates and Iminopyrrolidinates: Understanding Precursor Thermolysis to Design a Better Ligand. *Coord. Chem. Rev.* **2013**, *257*, 3192−3201.

(42) Rubel, O.; Baranovskii, S. D. Formation Energies of Antiphase Boundaries in GaAs and GaP: An Ab Initio Study. *Int. J. Mol. Sci.* **2009**, *10*, 5104−5114.

(43) Starr, D. E.; Campbell, C. T. Large Entropy Difference between Terrace and Step Sites on Surfaces. *J. Am. Chem. Soc.* **2008**, *130*, 7321−7327.

(44) Krischok, S.; Yanev, V.; Balykov, O.; Himmerlich, M.; Schaefer, J. A.; Kosiba, R.; Ecke, G.; Cimalla, I.; Cimalla, V.; Ambacher, O.; et al. Investigations of MBE Grown InN and the Influence of Sputtering on the Surface Composition. *Surf. Sci.* **2004**, *566−568*, 849−855.

(45) Veal, T. D.; King, P. D. C.; Jefferson, P. H.; Piper, L. F. J.; McConville, C. F.; Lu, H.; Schaff, W. J.; Anderson, P. A.; Durbin, S. M.; Muto, D.; et al. In Adlayers on C-Plane InN Surfaces: A Polarity-Dependent Study by x-Ray Photoemission Spectroscopy. *Phys. Rev. B: Condens. Matter Mater. Phys.* **2007**, *76*, 075313.

(46) Wu, C. L.; Lee, H. M.; Kuo, C. T.; Chen, C. H.; Gwo, S. Absence of Fermi-Level Pinning at Cleaved Nonpolar InN Surfaces. *Phys. Rev. Lett.* **2008**, *76*, 075313.

(47) Nagata, T.; Koblmüller, G.; Bierwagen, O.; Gallinat, C. S.; Speck, J. S. Surface Structure and Chemical States of A-Plane and c-Plane InN Films. *Appl. Phys. Lett.* **2009**, *95*, 132104.

(48) Wang, J. B.; Li, Z. F.; Chen, P. P.; Lu, W.; Yao, T. Raman Study of Gap Mode and Lattice Disorder Effect in InN Films Prepared by Plasma-Assisted Molecular Beam Epitaxy. *Acta Mater.* **2007**, *55*, 183−187.

(49) Frisch, M. J.; Trucks, G. W.; Schlegel, H. B.; Scuseria, G. E.; Robb, M. A.; Cheeseman, J. R.; Scalmani, G.; Barone, V.; Mennucci, B.; Petersson, G. A.; Nakatsuji, H.; Caricato, M.; Li, X.; Hratchian, H. P.; Izmaylov, A. F.; Bloino, J.; Zheng, G.; Sonnenberg, J. L.; Hada, M.; Ehara, M.; Toyota, K.; Fukuda, R.; Hasegawa, J.; Ishida, M.; Nakajima, T.; Honda, Y.; Kitao, O.; Nakai, H.; Vreven, T.; Montgomery, J. A., Jr.; Peralta, J. E.; Ogliaro, F.; Bearpark, M.; Heyd, J. J.; Brothers, E.; Kudin, K. N.; Staroverov, V. N.; Kobayashi, R.; Normand, J.; Raghavachari, K.; Rendell, A.; Burant, J. C.; Iyengar, S. S.; Tomasi, J.; Cossi, M.; Rega, N.; Millam, J. M.; Klene, M.; Knox, J. E.; Cross, J. B.; Bakken, V.; Adamo, C.; Jaramillo, J.; Gomperts, R.; Stratmann, R. E.; Yazyev, O.; Austin, A. J.; Cammi, R.; Pomelli, C.; Ochterski, J. W.; Martin, R. L.; Morokuma, K.; Zakrzewski, V. G.; Voth, G. A.; Salvador, P.; Dannenberg, J. J.; Dapprich, S.; Daniels, A. D.; Farkas, O.; Foresman, J. B.; Ortiz, J. V.; Cioslowski, J.; Fox, D. J. *Gaussian 16*, revision B.01; Gaussian, Inc.: Wallingford, CT, 2016.

(50) Becke, A. D. Density-Functional Thermochemistry. III. The Role of Exact Exchange. *J. Chem. Phys.* **1993**, *98*, 5648−5652.

(51) Lee, C.; Yang, W.; Parr, R. G. Development of the Colle-Salvetti Correlation-Energy Formula into a Functional of the Electron Density. *Phys. Rev. B: Condens. Matter Mater. Phys.* **1988**, *37*, 785−789.

(52) Grimme, S.; Antony, J.; Ehrlich, S.; Krieg, H. A Consistent and Accurate Ab Initio Parametrization of Density Functional Dispersion Correction (DFT-D) for the 94 Elements H-Pu. *J. Chem. Phys.* **2010**, *132* (15), 154104.

(53) Weigend, F.; Ahlrichs, R. Balanced Basis Sets of Split Valence, Triple Zeta Valence and Quadruple Zeta Valence Quality for H to Rn: Design and Assessment of Accuracy. *Phys. Chem. Chem. Phys.* **2005**, *7*, 3297−3305.

(54) Metz, B.; Stoll, H.; Dolg, M. Small-Core Multiconfiguration-Dirac-Hartree-Fock-Adjusted Pseudopotentials for Post-d Main Group Elements: Application to PbH and PbO. *J. Chem. Phys.* **2000**, *113*, 2563−2569.